

Surface hopping in laser-driven molecular dynamics

T. Fiedlschuster,^{1,2} J. Handt,¹ E. K. U. Gross,² and R. Schmidt^{1,*}

¹*Institut für Theoretische Physik, Technische Universität Dresden, D-01062 Dresden, Germany*

²*Max-Planck-Institut für Mikrostrukturphysik, Weinberg 2, D-06120 Halle, Germany*

(Received 23 August 2016; revised manuscript received 7 June 2017; published 28 June 2017)

A theoretical justification of the empirical surface hopping method for the laser-driven molecular dynamics is given by utilizing the formalism of the exact factorization of the molecular wave function [Abedi *et al.*, *Phys. Rev. Lett.* **105**, 123002 (2010)] in its quantum-classical limit. Employing an exactly solvable H_2^+ -like model system, it is shown that the deterministic classical nuclear motion on a single time-dependent surface in this approach describes the same physics as stochastic (hopping-induced) motion on several surfaces, provided Floquet surfaces are applied. Both quantum-classical methods do describe reasonably well the exact nuclear wave-packet dynamics for extremely different dissociation scenarios. Hopping schemes using Born-Oppenheimer surfaces or instantaneous Born-Oppenheimer surfaces fail completely.

DOI: [10.1103/PhysRevA.95.063424](https://doi.org/10.1103/PhysRevA.95.063424)

I. INTRODUCTION

For more than two decades, surface hopping (SH) [1] has been among the most popular and successful methods to describe nonadiabatic phenomena in atomic many-body systems (for reviews, see Refs. [2–5]). From the theoretical point of view, however, any SH scheme is inherently a phenomenological approach. The *ad hoc* assumption of stochastic jumps between electronic potential energy surfaces (PES) has, so far, never been rigorously deduced from the time-dependent Schrödinger equation (TDSE) for electrons and nuclei, and even the choice of the applied PES is ambiguous.

Very recently, however, first attempts have been made to justify the SH methodology on Born-Oppenheimer surfaces (BOSs), solely for the laser-free nonadiabatic dynamics [6–9]. A close similarity between the exact wave-packet propagation and SH on BOSs has been found in the framework of the exact factorization of the molecular wave function [6]. In this theory, the so-called exact time-dependent potential energy surface (EPES), together with an exact time-dependent vector potential, governs the true nuclear wave packet dynamics. The EPES can exhibit nearly discontinuous steplike features, just in the vicinity of avoided crossings between BOSs, leading simultaneously to acceleration and deceleration of certain parts of the quantum wave packet and resulting in its splitting. In close analogy, the SH mechanism can create branches of classical trajectories at avoided crossings. The findings [6] justify, albeit qualitatively but anyhow convincingly, the SH methodology on BOSs, in the field-free case.

For the laser-driven dynamics, any validation of SH is still lacking and the appropriate choice of the applicable PES is discussed controversially at present [10–12]. In fact, the hitherto purely intuitively chosen PES in SH models are fundamentally different from each other, and include BOSs [10,13–17], instantaneous BOSs (IBOSs) [18–22], as well as Floquet surfaces (FSs) [22–24]. From the massive differences in definition and properties of these PES, one can hardly expect that the appendant SH schemes can describe the same physics.

Obviously, the situation requires clarification and the general questions persist: Is there any validation of SH methodology *at all* in this case, and if yes, what are the adequate PES?

In this paper, we will provide answers to both questions employing the quantum-classical limit of the exact factorization [6,25–27] and using deliberately an exactly solvable model system. The exact factorization leads to a TDSE for the nuclear subsystem *alone* which is exact in the sense that the absolute square of the corresponding, purely nuclear, wave function yields the exact nuclear N -body density of the full electron-nuclear system. Hence, if the true quantum-mechanical nuclear density is approximated by an ensemble of classical trajectories, the correct classical force on the nuclei is *uniquely* given by the gradient of the EPES. In other words, the EPES contains all electron-nuclear correlations which generally can be retained in the quantum-classical limit of the TDSE. Consequently, ensembles of classical trajectories on the EPES can serve as judge for all the phenomenological SH models.

From the present comparative numerical studies, it will become apparent that the role of the BOSs in the field-free case is taken over by FSs in the laser-driven case, although the mechanism is more complex. Ensembles of classical trajectories, propagated stochastically on FSs (Floquet-SH, F-SH) and deterministically on the EPES (exact surface dynamics, ESD), do describe the same physics. Moreover, in the considered cases, the results are in excellent agreement with those of the TDSE. Complementary SH calculations with BOSs (BO-SH) and IBOSs (IBO-SH) deliver unphysical results.

The paper is organized as follows: In Sec. II, the theoretical background is summarized, i.e., the utilized model system and its relevant PES (Sec. II A), the hopping methods on different PES (Sec. II B), and the exact factorization theory and its application in the quantum-classical limit (Sec. II C).

In Sec. III, extensive comparative numerical results for different dissociation scenarios are presented applying all three SH methods (BO-SH, IBO-SH, F-SH), the ESD, as well as the TDSE. In Sec. IV, the findings are summarized. Appendix A contains a discussion of the choice of classical initial conditions in quantum-classical trajectory calculations.

*ruediger.schmidt@tu-dresden.de

In Appendix B, numerical details are presented. Several movies are provided as Supplemental Material to this paper [28]. They contain visualizations of the time dependence of PES and nuclear densities. The movies are briefly described in Appendix C.

Atomic units are used unless stated otherwise.

II. THEORY

A. Model system and potential energy surfaces

We use a numerically exactly solvable two-dimensional H_2^+ -like model and a linear polarized laser in dipole approximation for all exemplary calculations in this paper. In the center-of-mass frame, the soft-core Hamiltonian of this model system reads

$$H = -\frac{\Delta_R}{2M} - \frac{\Delta_r}{2} + \frac{1}{R+0.03} - \mu F(t)\cos(\omega t) - \frac{1}{\sqrt{(r-R/2)^2+1}} - \frac{1}{\sqrt{(r+R/2)^2+1}}, \quad (1)$$

with M the reduced nuclear mass, R the internuclear distance, and r the electronic position operator. The laser-molecule interaction (laser frequency $\omega = 0.2$ a.u. [$\lambda \approx 225$] nm throughout the whole paper) is included in the length gauge (dipole operator $\mu = -r$). We apply laser fields where the envelope $F(t)$ does not change considerably during one optical cycle $T = 2\pi/\omega \approx 0.8$ fs.

We calculate BO surfaces $E_i^{\text{BO}}(R)$ by diagonalizing the fixed-nuclei field-free Hamiltonian

$$H^{\text{BO}}(R) = -\frac{\Delta_r}{2} + \frac{1}{R+0.03} - \frac{1}{\sqrt{(r-R/2)^2+1}} - \frac{1}{\sqrt{(r+R/2)^2+1}}. \quad (2)$$

The relatively low laser intensities ($I \leq 10^{13}$ W/cm²) considered in this paper allow us to focus on the two lowest BO surfaces $E_0^{\text{BO}}(R)$ and $E_1^{\text{BO}}(R)$. The corresponding BO states $|\varphi_{0/1}(R)\rangle$ are strongly coupled to each other via the dipole matrix element $\langle\varphi_0(R)|\mu|\varphi_1(R)\rangle = \mu_{01}^{\text{BO}}(R) \approx R/2$, but only weakly coupled to BO states with $i > 1$.

The time-dependent IBO surfaces $E_{0/1}^{\text{IBO}}(R,t)$, eigenvalues of the fixed-nuclei Hamiltonian *including* the laser

$$H^{\text{IBO}}(R) = H^{\text{BO}}(R) - \mu F(t)\cos\omega t, \quad (3)$$

can be calculated as

$$E_{0/1}^{\text{IBO}}(R,t) = E_{0/1}^{\text{BO}}(R)\cos^2\theta(R,t) + E_{1/0}^{\text{BO}}(R)\sin^2\theta(R,t) \pm \mu_{01}^{\text{BO}}(R)F(t)\cos(\omega t)\sin 2\theta(R,t) \quad (4)$$

with the mixing parameter

$$\theta(R,t) = \frac{1}{2} \arctan \frac{2\mu_{01}^{\text{BO}}(R)F(t)\cos(\omega t)}{E_0^{\text{BO}}(R) - E_1^{\text{BO}}(R)}. \quad (5)$$

Floquet surfaces $E^{\text{F}}(R,t)$, time dependent only via the envelope $F(t)$ of the laser, are calculated by diagonalizing the Floquet matrix [29,30] (for details, see also Ref. [24]).

Figure 1 shows the two lowest BOSs, the corresponding IBOSs, and two relevant FSs for the model system (1) using

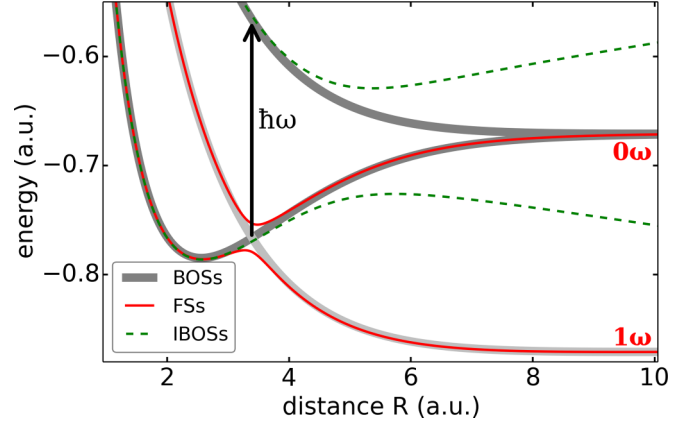


FIG. 1. The two lowest BOSs and IBOSs (for $|\cos\omega t| = 1$), the excited BOS shifted down by $\hbar\omega$ (light gray), as well as the two FSs (0ω and 1ω FS) forming the one-photon crossing for a $\lambda = 225$ nm laser with $I = 10^{13}$ W/cm². The vertical arrow of length $\hbar\omega$ marks the one-photon resonance between the BOSs.

a laser intensity of $I = 10^{13}$ W/cm². The different time dependence of the PES is visualized in the Supplemental Material [28]. The displayed PES look very different, although they do have some common aspects: The IBOSs are identical with the BOSs whenever $\cos\omega t = 0$. The FSs are piecewise BOSs, appropriately shifted by the photon energy $\hbar\omega$ (dressed BOSs). The decisive difference between the PES concerns their behavior just at the one photon resonance located at $R \approx 3.5$ a.u. Whereas BOSs and IBOSs do not show any peculiarities, the FSs exhibit an avoided crossing. These typical crossings are the crucial difference to all other PES. The resulting gap size (even tunable by the electric field strength) allows for both deterministic evolution on one FS surface (without hops) or stochastic dynamics on both FS (with hops). To what extent this peculiarity favors the use of FSs in corresponding SH schemes will be analyzed in the comprehensive dynamical calculations in Sec. III.

B. Surface hopping methods on different PES (BO-SH, IBO-SH, F-SH)

In Sec. III, we will compare numerical results obtained with different hopping methods, namely BO-SH (hopping between BOSs), IBO-SH (hopping between IBOSs), and F-SH (hopping between FSs). All these hopping methods are based on Tully's fewest switching algorithm [1], where the time evolution of an electronic wave function determines the hopping probability for classical nuclear trajectories between different PES. Details of the hopping methods and their numerical implementation are given and discussed in our previous work for BO-SH [31–34] and F-SH [24]. For IBO-SH, we adopt the method presented in Refs. [19,20].

As discussed in Sec. II A, the various PES are quite different. In addition, the hopping schemes using these surfaces differ considerably in the way how hops are performed. If a hop occurs in BO-SH, the trajectory is set onto the new BO surface. The momentum of the trajectory is strictly conserved, assuming that the energy difference before and after the hop is provided by the laser field [35]. If a hop occurs in

F-SH, the trajectory is set onto the new Floquet surface. The laser-molecule interaction is incorporated into the Floquet surfaces, and thus the energy is strictly conserved. Therefore, the momentum after the hop is adjusted to match the new kinetic energy. If a hop would result in negative kinetic energy, it is considered classically forbidden and rejected. If a hop occurs in IBO-SH, the trajectory is set onto the new IBO surface. The use of IBO-SH comes with some peculiarities concerning energy and momentum conservation. We apply the ratio method, developed in Ref. [20]. This method proposes a weighted conservation of energy and momentum, based on the ratio of different contributions to the hopping probability (see Sec. 3 in Ref. [20]). The ratio method manages to connect special cases of strict momentum and strict energy conservation, resulting, however, in neither strict momentum nor strict energy conservation for most cases. Hops which result in negative kinetic energy are rejected.

C. The exact factorization theory and propagation on the EPES

In this section, we briefly summarize the exact factorization theory of the time-dependent electron-nuclear wave function [25,36], the calculation of the EPES, and the classical equations of motion in the quantum-classical limit of the theory.

The full wave function, to be obtained by numerically solving the TDSE for our model system (1), is factorized to read

$$\psi(R, r, t) = \chi(R, t) \phi_R(r, t), \quad (6)$$

with a nuclear part

$$\chi(R, t) = e^{iS(R, t)} \sqrt{\int dr |\psi(R, r, t)|^2}, \quad (7)$$

and an electronic part

$$\phi_R(r, t) = \frac{\psi(R, r, t)}{\chi(R, t)}. \quad (8)$$

The phase $S(R, t)$ is determined in a gauge with vanishing vector potential

$$A(R, t) = -i \int dr \phi_R^*(r, t) \partial_R \phi_R(r, t) = 0 \quad (9)$$

and reads

$$S(R, t) = \int_{R_0}^R dR' \frac{\text{Im} \left\{ \int dr \psi(R', r, t) \partial_{R'} \psi(R', r, t) \right\}}{|\chi(R', t)|^2}. \quad (10)$$

In the same gauge, the EPES is calculated as (see Ref. [36])

$$\epsilon(R, t) = i \frac{\partial_t \chi(R, t)}{\chi(R, t)} + \frac{\Delta_R \chi(R, t)}{2M \chi(R, t)}. \quad (11)$$

In the quantum-classical limit, the exact force on the nuclei is given by the gradient of the EPES. We use this to perform ESD calculations (deterministic propagation of classical nuclear trajectories on the EPES obtained from the TDSE solution of the specific scenarios) for our comparative numerical studies in Sec. III.

The EPES may still be shifted (globally) by a constant to fix the gauge entirely. We use this later to shift the EPES

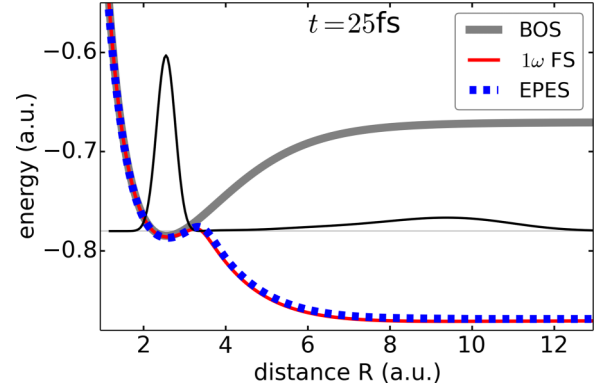


FIG. 2. Wave packet of the TDSE for scenario 1 (thin black line), together with the ground-state BOS, the 1ω FS, and the EPES at $t = 25$ fs.

towards the Floquet surfaces in Figs. 2 and 4. Furthermore, for the comparison of Floquet surfaces and EPES, the latter is averaged over one optical cycle of the laser $T = 2\pi/\omega \approx 0.8$ fs. The averaged EPES reads

$$\tilde{\epsilon}(R, t) = \frac{1}{T} \int_{-T/2}^{T/2} dt' \epsilon(R, t'). \quad (12)$$

The difference between ϵ and $\tilde{\epsilon}$ mainly consists in an oscillation of ϵ around $\tilde{\epsilon}$ with twice the laser frequency and an R -dependent amplitude (see also the visualization in the Supplemental Material [28]).

III. RESULTS

To validate surface hopping for laser-driven molecular dynamics and to unambiguously demonstrate the differences between surface hopping using BO surfaces, IBO surfaces, and Floquet surfaces, we present exemplary calculations for generic scenarios of molecular dissociation in this section. In these calculations, we will consider the most detailed observable quantity of all, namely the resulting nuclear probability density in position and momentum space. This allows for a direct comparison of the quantum-classical dynamics with the exact wave-packet dynamics of the TDSE and excludes artificial agreement between the different methods in (possibly) insensitive integral quantities. For the classical initial conditions, we use the Wigner distributions of the exact initial quantum wave packets (see Appendix A). The various methods to be applied are outlined Sec. II (and references therein); additional information about the numerical implementation is given in Appendix B.

In the following, we will consider various dissociation scenarios with initial conditions which ensure extremely different mechanisms.

A. Scenario 1 (photon absorption)

The first scenario is designed to steer the molecule into the bond-softening dissociation channel. The H_2^+ -like molecule ($M = 918$ a.u.) is initially in the electronic ground state. The nuclei are assumed to be in an excited state constructed by providing an additional momentum of -2.5 a.u. to the vibrational

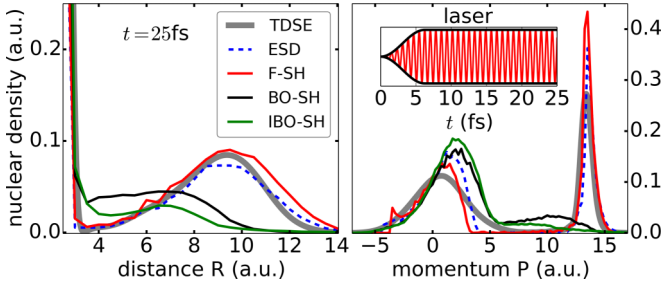


FIG. 3. The nuclear densities for scenario 1 at $t = 25$ fs, obtained by solving the TDSE and with the different quantum-classical methods, in position (left panel) and momentum space (right panel). In the inset, the electric field and the envelope of the laser are shown.

ground state $\nu = 0$. This choice guarantees both a sufficiently large bond-softening dissociation probability together with classical initial conditions in terms of positive Wigner distributions (Appendix A). Pronounced bond-softening dissociation probabilities can also be realized by starting with certain excited vibrational eigenstates, for which, however, the Wigner distributions are not positive (Appendix A). The molecule is exposed to a cw laser with $I = 10^{13}$ W/cm² (same as used for Fig. 1), switched on with a sin²-shaped ramp (see inset in Fig. 3).

We will first discuss the exact quantum-mechanical propagation of the system. In Fig. 2, the resulting wave packet of the TDSE at $t = 25$ fs is shown. Most of the initial wave packet remains bound, localized at the equilibrium distance at $R \approx 2.5$ a.u. The dissociating part exhibits a maximum at $R \approx 9$ a.u. In Fig. 3, it is presented together with the momentum distribution of the whole wave packet. The dissociating part is sharply localized at $P \approx 13.5$ a.u. The corresponding kinetic energy release of the fragments of $P^2/2M \approx 0.1$ a.u. equals the difference between the photon energy $\hbar\omega = 0.2$ a.u. and the binding energy of the molecule in its vibrational ground state of $E_0 \approx 0.1$ a.u. This perfect energy balance strongly suggests (although does not yet conclusively prove) that one photon absorption is the dominant dissociation mechanism. So much about the exact solution of the problem.

The interesting question now is how the EPES of this scenario, calculated from the exact solution of the TDSE, compares to the different PES discussed above and presented in Fig. 1. In Fig. 2, the ground-state BOS, the 1ω FS, and the EPES are shown at $t = 25$ fs. The EPES is averaged over one optical cycle of the laser; the whole time dependence of the EPES and of the 1ω FS is visualized in the Supplemental Material [28]. Evidently, and indeed surprisingly, the averaged EPES and the 1ω FS coincide perfectly at all distances and all times. Hence, the deterministic quantum-classical dynamics on both surfaces is definitely the same. To a large extent, this should hold also for an ensemble of trajectories in ESD and full F-SH calculations, as long as the number of hops per trajectory N between FS remains very small ($N \ll 1$). This is indeed the case (see Table I) and can also be expected from the discussion of Fig. 1. Hence, and now not surprisingly, the nuclear densities obtained with ESD and full F-SH calculations are nearly equal (see Fig. 3). In addition, they do compare nicely with that of the TDSE in position as well as in momentum space. Finally,

TABLE I. The average number of hops per trajectory in the different surface hopping methods for the investigated scenarios.

Method	Scenario 1 (cw)	Scenario 2a (pulse)	Scenario 2b (cw)
BO-SH	2.6	1.0	15.7
IBO-SH	2.9	2.5	55.9
F-SH	0.01	0.6	0.7

the analysis of the dynamics in terms of FSs confirms directly the upper assumed one-photon absorption mechanism.

The nuclear densities calculated with BO-SH and IBO-SH are in striking qualitative disagreement with that obtained by the other methods (see Fig. 3). In position space, no distinct maximum around $R = 9$ a.u. is present. In momentum space, the high-energetic peak around $P = 13.5$ a.u. is totally missing. Any dissociation of the molecule on these surfaces requires stringently a certain number of hops (see Fig. 1), which do occur (see Table I) but, at the same time, lead to fundamentally different nuclear dynamics.

Summarizing this part, we found, somewhat surprisingly, that the EPES can coincide with a single FS. In this case, the nonadiabatic dynamics proceeds deterministically, i.e., without any hops in the F-SH procedure. In the following, we will consider a scenario where hops between FSs stringently do occur.

B. Scenario 2a (photon emission in a laser pulse)

A Na₂⁺-like molecule ($M = 23 \times 918$ a.u.) is initially lifted into its first excited electronic state (first excited BO state). The initial nuclear state is the Franck-Condon projection of the vibrational ground state $\nu = 0$ onto the eigenstates of the nuclei in the potential energy surface of the excited electronic state (see wave packet at $t = 0$ in Fig. 4). The molecule is exposed to a short Gaussian-shaped laser pulse of 7 fs duration (full width at half maximum of the intensity), wavelength of $\lambda = 225$ nm, and peak intensity of $I = 3 \times 10^{12}$ W/cm² (see inset in Fig. 5). The laser envelope is tuned such that the wave packet passes the one-photon resonance when the maximal intensity is reached, which itself is chosen such that the wave

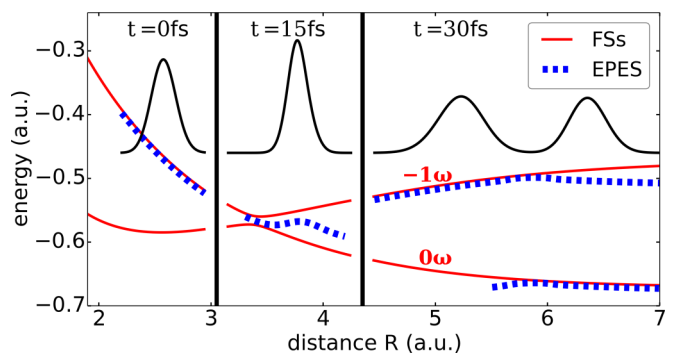


FIG. 4. Wave packet of the TDSE for scenario 2a (snapshots at $t = 0, 15,$ and 30 fs; thin black lines with different scales), together with the relevant FSs and the EPES. For $R > 5.5$ a.u., the EPES is also plotted shifted down to the 0ω FS.

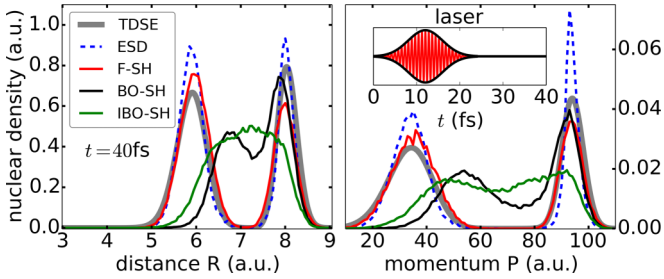


FIG. 5. The nuclear densities for scenario 2a at $t = 40$ fs, obtained by solving the TDSE and with the different quantum-classical methods, in position (left panel) and momentum space (right panel). In the inset, the electric field and the envelope of the laser pulse are shown.

packet splits into two nearly equal parts during the dynamics [37].

Again, we will first discuss the exact wave-packet dynamics resulting from the TDSE. It is depicted at different times $t = 0, 15, 30$ fs in Fig. 4. The final nuclear densities of the TDSE in position and momentum space are given in Fig. 5, at $t = 40$ fs. As clearly seen, the initial wave packet is split into a fast-moving part (with mean momentum of $P \approx 95$ a.u.) and a slow-moving part (with $P \approx 35$ a.u.). The mean kinetic energy of the fast one $P^2/2M \approx 0.21$ a.u. corresponds to the energy difference on the excited BOS between the initial mean internuclear distance of $R \approx 2.5$ a.u. ($E \approx -0.46$ a.u.) and the final one of $R \approx 8$ a.u. ($E \approx -0.67$ a.u.), reflecting free motion (sliding down) on this surface as dissociation mechanism. On the other hand, the mean kinetic energy of the retarded part $P^2/2M \approx 0.03$ a.u. is smaller by almost one photon energy $\hbar\omega = 0.2$ a.u., suggesting (but not definitely proving) stimulated photon emission as the dissociation mechanism for this fraction of the wave packet.

In Fig. 4, snapshots of the corresponding EPES as well as of the 0ω and -1ω FSs are presented (a time-dependent visualization is given in the Supplemental Material [28]). Field-free FSs are generally identical with BOSs, dressed by a certain number of photons. The EPES, respectively its gradient, also coincides with BOSs, in the field-free case [6]. Thus, at $t = 0$ the first excited BOS is equal to the EPES as well as the -1ω FS (in our notation). The 0ω FS equals the ground-state BOS, dressed (shifted up) by one photon. After the pulse at $t = 30$ fs, the FSs change their assignment with respect to the (dressed) BOSs. The EPES, however, and indeed somewhat surprisingly, coincides with the (one-photon-shifted) ground-state BOS (and the -1ω FS) in the range of the retarded part of the wave packet, and with the excited BOS (and the 0ω FS) in the region of the fast-moving part. We note in passing that this already proves the interpretation of the dissociation mechanisms for both parts of the wave packet given above.

During the laser pulse ($t = 15$ fs in Fig. 4), the EPES does not coincide with one of the other surfaces. Its alternating gradients lead, at the same time, to acceleration and deceleration of certain parts of the wave packet of the TDSE, resulting in the splitting of the wave packet. This pure quantum mechanical effect survives the crude

quantum-classical approximation in terms of decelerated and accelerated classical trajectories in appendant ESD calculations, which is convincingly demonstrated in Fig. 5. The nuclear densities, resulting from the deterministic ESD calculations, are in excellent agreement with that of the TDSE in position as well as in momentum space.

As an important result of this work, it will be shown in the following that the same mechanism can be clearly understood and adequately described also with the stochastic SH methodology, provided FSs are applied. In Fig. 4, both relevant FSs are shown at $t = 15$ fs. They exhibit a typical avoided crossing located at the one photon resonance ($R \approx 3$ a.u.). This crossing induces a strong nonadiabatic coupling between both surfaces. Thus, in classical F-SH calculations, trajectories staying on the upper FS are decelerated owing to the loss of one photon. Trajectories performing one hop between the upper and lower FS are further accelerated and slide down the initial excited BOS. The almost equal partition of both types of trajectories (see number of hops per trajectory in Table I) will lead to an almost symmetric splitting of the nuclear density in position space with two pronounced maxima in momentum space. The results of the dynamical F-SH calculations are in intriguing agreement with ESD calculations as well as the TDSE solution (see Fig. 5).

Avoided crossings, located at photon resonances, basically do not exist between BOSs and IBOSs, owing to their photonless definition. On the other side, it is just the additional nonadiabatic coupling $\sim \dot{R} \langle \Phi_{-1\omega} | \partial_R \Phi_{0\omega} \rangle$ between the Floquet states $|\Phi\rangle$, which leads to the different dissociation mechanisms [24]. Hence, it is not very surprising that the SH calculations with BOSs or IBOSs yield nuclear densities which disagree, even qualitatively, with that of F-SH (see Fig. 5). In these approaches, hops are (mainly) created by the laser-induced coupling ($\sim R F(t) \cos \omega t$ for BOSs [24]; see Ref. [19] for IBOSs) and do occur at all internuclear distances. Accordingly, the number of hops is distinctly larger than in the F-SH approach (middle column in Table I).

C. Scenario 2b (photon emission in a cw-like laser)

To further examine the different SH methods, we repeat the dynamical calculations of scenario 2a, but replace the short laser pulse by a cw-like laser (see inset in Fig. 6). From the discussion above, the results of the F-SH calculations are expected to remain largely unaffected by this change, because the whole dissociation process is determined during a short time interval of about 15 fs where both laser fields

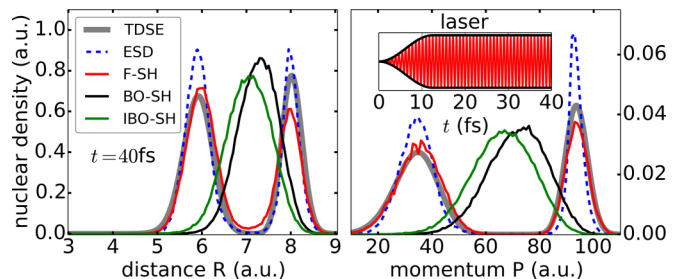


FIG. 6. The nuclear densities for scenario 2 at $t = 40$ fs, using a cw-like laser (see inset) instead of a finite pulse.

are practically equal (cf. insets in Figs. 5 and 6). Indeed, the calculated nuclear densities are nearly identical with that obtained for the short laser pulse (cf. nuclear densities in Figs. 5 and 6). In addition, they do agree nicely with that of the TDSE and ESD. In striking contrast, the nuclear densities calculated with BO-SH or IBO-SH for the cw-like laser are drastically different from that obtained for the short pulse (cf. Figs. 5 and 6). This unphysical behavior results from the artificial large number of hops (see last column in Table I) which, in addition, will further increase in time (up to $N \rightarrow \infty!$) in both approaches.

IV. SUMMARY AND OUTLOOK

We have performed a comprehensive study of the laser-driven dynamics, using different quantum-classical approximations of the TDSE for electrons and nuclei. We have shown that the inherently deterministic propagation of the nuclei on the EPES can be well described by stochastic motion on several surfaces mediated by hops between them, provided FSs are used. Both methods (ESD and F-SH) deliver the same results which, in addition, are in excellent agreement with the exact wave-packet dynamics of the full electron-nuclear TDSE. The studies justify the SH methodology for the laser-driven case. At the same time, the investigations also conclude the present, controversially led debate about the applicability of BOSs or IBOSs in SH schemes [10–12], because both are not appropriate. These conclusions are valid for (and at the same time limited to) laser fields where the Floquet treatment of the time-dependent Hamiltonian approximately applies.

Whereas the solution of the full electron-nuclear TDSE is restricted to small model systems, the SH approach can be applied to realistic systems and should, as we have shown, reproduce the correct laser-driven dynamics as long as the stochastic hopping is done between Floquet surfaces.

ACKNOWLEDGMENT

We gratefully acknowledge financial support from the Deutsche Forschungsgemeinschaft through the Normalverfahren (Nr. SCHM 957/10-1).

APPENDIX A: CLASSICAL INITIAL CONDITIONS

In Sec. III, we compare quantum-classical nuclear densities (obtained with different quantum-classical methods) with the exact quantum-mechanical nuclear density (obtained by solving the TDSE). This comes with some constraints in the initial conditions. The appropriate choice of initial conditions for an ensemble of classical nuclear trajectories in a quantum-classical calculation is a fundamental question of general interest, which we do not want to address here. Focusing on the nuclear probability density as observable, however, the initial conditions must lead to a quantum-classical nuclear density identical to the nuclear density of the corresponding quantum state, at $t = 0$. One way to satisfy this is to sample the classical initial conditions (in phase space $\{R, P\}$) from the Wigner

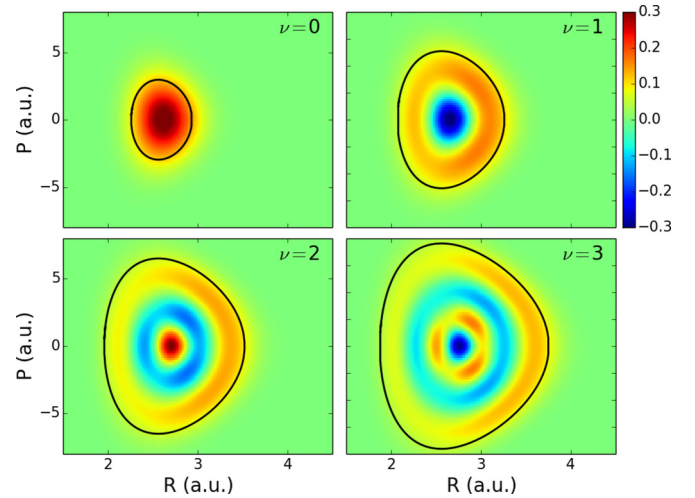


FIG. 7. The Wigner distribution for the vibrational states $\nu = 0, 1, 2, 3$ for the H_2^+ -like model. The black line shows the accessible phase space for a classical trajectory propagated in the BO ground-state surface with the corresponding vibrational energy E_ν .

distribution of the initial nuclear quantum state $\varphi(R, t_0)$,

$$W_{\varphi(t_0)}(R, P) = 2\pi \int dQ e^{-iPQ} \varphi\left(R + \frac{Q}{2}, t_0\right) \times \varphi^*\left(R - \frac{Q}{2}, t_0\right). \quad (\text{A1})$$

The reader not familiar with the Wigner distribution is encouraged to have a look at Ref. [38]. $W(R, P)$ fulfills

$$\int dP W_{\varphi(t)}(R, P) = |\varphi(R, t)|^2 \quad (\text{A2})$$

and

$$\int dR W_{\varphi(t)}(R, P) = |\varphi(P, t)|^2, \quad (\text{A3})$$

such that the quantum-classical nuclear densities at $t = 0$ are identical to the nuclear density of the initial quantum state, in position space as well as in momentum space. The time-dependent Wigner distribution can be obtained by solving the TDSE for the corresponding state $|\varphi(t)\rangle$, or by solving the Wigner-Liouville equation for $W_{\varphi(t=0)}(R, P)$ (see Ref. [38]).

In Fig. 7, the Wigner distributions of the first four vibrational states for our H_2^+ -like model are shown. It becomes apparent that the phase space distribution $W(R, P)$ is remarkably different compared to the phase space accessible by a classical trajectory, propagated in the ground-state BOS with the corresponding vibrational energy E_ν . Figure 7 furthermore reveals that the Wigner distribution is negative in wide phase space regions for $\nu = 1, 2, 3$. These large regions of negative values are well understandable, since the Wigner distributions of orthogonal quantum states are orthogonal,

$$\langle \varphi_1 | \varphi_2 \rangle = 0 \Leftrightarrow \int dR dP W_{\varphi_1} W_{\varphi_2} = 0. \quad (\text{A4})$$

Thus, with the positive Wigner distribution of the vibrational ground state $\nu = 0$, the Wigner distributions of all excited vibrational states will take negative values in

considerable phase space volumes to satisfy (A4). The role of positive and negative values in $W(R, P)$ is crucial when calculating observables, e.g., the nuclear densities (A2) and (A3). Even in cases where the full Wigner-Liouville dynamics only marginally deviates from purely classical dynamics, the balance of positive and negative trajectories is disturbed. The predictions for observables, calculated by an ensemble of classical trajectories, become physically meaningless. This restricts quantum-classical calculations to initial quantum states with positive Wigner distributions. A valid choice is the vibrational state $\nu = 0$, or any wave packet which leads to a positive Wigner distribution, e.g., the initial states used in Sec. III.

APPENDIX B: NUMERICAL DETAILS

1. Numerical solution of the TDSE

To obtain the full time-dependent electron-nuclear wave function for the calculation of the EPES and the quantum-mechanical nuclear probability density, we solve the TDSE

$$i\partial_t\psi(R,r,t) = H(R,r,t)\psi(R,r,t) \quad (\text{B1})$$

for the model system defined by the Hamiltonian (1) using the second-order split-operator method on a grid. The grid spans from $R = 0$ a.u. to $R = 20$ a.u. for the nuclear bond length and from $r = -20$ a.u. to $r = 20$ a.u. for the electronic coordinate. This small grid is sufficient for the investigated examples. To prevent unphysical reflections, the values of the wave function near the grid boundaries are damped by an absorber function. For the H_2^+ -like model ($M = 918$ a.u.), we use 512 grid points for the electron as well as the nuclei. For the Na_2^+ -like model ($M = 23 \times 918$ a.u.), we use 512 grid points for the electron and 32×512 grid points for the nuclei. The relatively large number of nuclear grid points is due to the larger nuclear momenta and necessary for convergence of the calculation of the EPES. We use a time step of $\Delta t = 0.1$ a.u. in all cases.

2. Details for the surface hopping calculations (BO-SH, IBO-SH, F-SH)

To obtain the quantum-classical nuclear densities with BO-SH, IBO-SH, and F-SH, an ensemble of $N = 100\,000$ independent classical trajectories is propagated using the respective hopping scheme to mimic the quantum-mechanical wave packet dynamics. The large number of trajectories is not necessary for convergence but favorable for binning and displaying the resulting nuclear probability densities. The classical initial conditions are discussed in Appendix A. The trajectories are propagated using the leap-frog algorithm with a time step $\Delta t = 0.01$ a.u. Simultaneously, for each trajectory, a TDSE for the electronic wave function is solved in basis expansion. Following Tully's fewest switching algorithm [1], the time evolution of this wave function determines the hopping probability between different PES. The electronic wave function is expanded into the two lowest BO states (BO-SH and IBO-SH) or into dressed BO states (F-SH; see Ref. [24]). This wave function is then transformed into the basis of IBO states for IBO-SH, and into Floquet states for F-SH. For more detailed information on the calculation of

the hopping probabilities and how hops are performed, see Sec. II B and references therein.

BO-SH is the numerically most efficient of the considered SH schemes, closely followed by IBO-SH. F-SH requires the use of a larger basis for the propagation of the electronic wave function, which leads to a larger numerical effort (in the examples for Sec. III, the computation time for a F-SH trajectory is about three times larger than for a BO-SH trajectory).

3. Details for the exact surface dynamics (ESD)

For the propagation of classical trajectories on the EPES, the same initial conditions and numerical parameters as for the surface hopping methods are used (see Sec. B 2). We note that, for the chosen laser parameters and nuclear masses, the nuclear probability densities obtained with classical trajectories propagated on the EPES ϵ and the time-averaged EPES $\bar{\epsilon}$ [see (11), resp. (12)] are practically identical.

APPENDIX C: VISUALIZATION OF PES AND NUCLEAR DENSITIES (MOVIES)

In this section, we briefly discuss the movies provided with the Supplemental Material [28].

The movie "figure1.mov" is a time-dependent version of Fig. 1. It shows BO, IBO, and Floquet surfaces for the H_2^+ -like model system for the first 10 fs of the laser used in scenario 1. The differences between the surfaces (time-independent BO surfaces, slowly time-dependent Floquet surfaces, and rapidly oscillating IBO surfaces) are apparent.

The movie "scenario1.mov" is a time-dependent version of Fig. 2. It shows the time-dependent nuclear density, obtained by solving the TDSE, alongside with the ground-state BO surface and the Floquet surface relevant for one-photon dissociation. The EPES as well as the EPES averaged over one optical cycle of the laser are shown in regions of nonvanishing nuclear density. While the oscillation of the EPES is similar to that of the IBO surfaces, the shape of the EPES is already clearly comparable to the Floquet surface. Averaging the EPES over one optical cycle yields a surface remarkably close to the Floquet surface, in shape and time dependence. For the chosen nuclear mass and laser parameters, the oscillation of the EPES has practically no impact on the classical nuclear dynamics.

The movie "scenario2.mov" is a time-dependent version of Fig. 4. Also this movie shows the time-dependent nuclear density, obtained by solving the TDSE, alongside with the ground-state BO surface and the two relevant Floquet surfaces. The EPES in regions of nonvanishing nuclear density is shown twice, clamped at the different Floquet surfaces. After the nuclear density passed the region of resonant one-photon emission, the EPES forms a cone, actively splitting the classical nuclear density propagated on it (not shown) into the two peaks also observed in the exact TDSE dynamics. The gradient of the EPES left (right) of the cone is practically identical to the gradient of the upper (lower) Floquet surface. As shown in Sec. III, F-SH also yields the correct splitting, due to the hopping during the laser pulse.

- [1] J. C. Tully, *J. Chem. Phys.* **93**, 1061 (1990).
- [2] J. C. Tully, *J. Chem. Phys.* **137**, 22A301 (2012).
- [3] M. Barbatti and R. Crespo-Otero, in *Density-Functional Methods for Excited States*, edited by N. Ferré, M. Filatov, and M. Huix-Rotllant (Springer, Cham, Switzerland, 2016), pp. 415–444.
- [4] J. E. Subotnik, A. Jain, B. Landry, A. Petit, W. Ouyang, and N. Bellonzi, *Annu. Rev. Phys. Chem.* **67**, 387 (2016).
- [5] L. Wang, A. Akimov, and O. V. Prezhdo, *J. Phys. Chem. Lett.* **7**, 2100 (2016).
- [6] A. Abedi, F. Agostini, Y. Suzuki, and E. K. U. Gross, *Phys. Rev. Lett.* **110**, 263001 (2013).
- [7] B. F. E. Curchod and I. Tavernelli, *J. Chem. Phys.* **138**, 184112 (2013).
- [8] J. E. Subotnik, W. Ouyang, and B. R. Landry, *J. Chem. Phys.* **139**, 214107 (2013).
- [9] R. Kapral, *Chem. Phys.* **481**, 77 (2016).
- [10] R. Mitrić, J. Petersen, and V. Bonacic-Koutecký, *Phys. Rev. A* **79**, 053416 (2009).
- [11] M. Richter, P. Marquetand, J. González-Vázquez, I. Sola, and L. González, *J. Chem. Theory Comput.* **7**, 1253 (2011); **8**, 374 (2012).
- [12] Y. Suzuki, A. Abedi, N. T. Maitra, and E. K. U. Gross, *Phys. Chem. Chem. Phys.* **17**, 29271 (2015).
- [13] G. A. Jones, A. Acocella, and F. Zerbetto, *J. Phys. Chem. A* **112**, 9650 (2008).
- [14] I. Tavernelli, B. F. E. Curchod, and U. Rothlisberger, *Phys. Rev. A* **81**, 052508 (2010).
- [15] R. Mitrić, J. Petersen, M. Wohlgemuth, U. Werner, V. Bonacic-Koutecký, L. Wöste, and J. Jortner, *J. Phys. Chem. A* **115**, 3755 (2011).
- [16] J. Petersen and R. Mitrić, *Phys. Chem. Chem. Phys.* **14**, 8299 (2012).
- [17] J. J. Bajo, G. Granucci, and M. Persico, *J. Chem. Phys.* **140**, 044113 (2014).
- [18] P. Dietrich, M. Y. Ivanov, F. A. Ilkov, and P. B. Corkum, *Phys. Rev. Lett.* **77**, 4150 (1996).
- [19] M. Thachuk, M. Y. Ivanov, and D. M. Wardlaw, *J. Chem. Phys.* **105**, 4094 (1996).
- [20] M. Thachuk, M. Y. Ivanov, and D. M. Wardlaw, *J. Chem. Phys.* **109**, 5747 (1998).
- [21] F. Kelkensberg, G. Sansone, M. Y. Ivanov, and M. Vrakking, *Phys. Chem. Chem. Phys.* **13**, 8647 (2011).
- [22] J. J. Bajo, J. González-Vázquez, I. R. Sola, J. Santamaria, M. Richter, P. Marquetand, and L. González, *J. Phys. Chem. A* **116**, 2800 (2012).
- [23] I. Horenko, B. Schmidt, and C. Schütte, *J. Chem. Phys.* **115**, 5733 (2001).
- [24] T. Fiedlschuster, J. Handt, and R. Schmidt, *Phys. Rev. A* **93**, 053409 (2016).
- [25] A. Abedi, N. T. Maitra, and E. K. U. Gross, *Phys. Rev. Lett.* **105**, 123002 (2010).
- [26] S. K. Min, A. Abedi, K. S. Kim, and E. K. U. Gross, *Phys. Rev. Lett.* **113**, 263004 (2014).
- [27] S. K. Min, F. Agostini, and E. K. U. Gross, *Phys. Rev. Lett.* **115**, 073001 (2015).
- [28] See Supplemental Material at <http://link.aps.org/supplemental/10.1103/PhysRevA.95.063424> for several movies described in Appendix C.
- [29] J. H. Shirley, *Phys. Rev.* **138**, B979 (1965).
- [30] H. Sambe, *Phys. Rev. A* **7**, 2203 (1973).
- [31] M. Fischer, J. Handt, and R. Schmidt, *Phys. Rev. A* **90**, 012525 (2014).
- [32] M. Fischer, J. Handt, and R. Schmidt, *Phys. Rev. A* **90**, 012526 (2014).
- [33] M. Fischer, J. Handt, and R. Schmidt, *Phys. Rev. A* **90**, 012527 (2014).
- [34] Decisive arguments against the use of BO-SH for laser-driven molecular dynamics have been discussed already in Refs. [31,33], albeit qualitatively. Here we use intentionally the general BO-SH formalism of Ref. [31] for the laser-driven case to prove the arguments quantitatively.
- [35] In our model system, the nonadiabatic coupling $D_{01} = \langle \varphi_0(R) | \partial_R \varphi_1(R) \rangle$ vanishes exactly thus *all* hops in BO-SH are due to the laser. The general case $D_{ij} \neq 0$ is discussed in Ref. [31].
- [36] A. Abedi, N. T. Maitra, and E. K. U. Gross, *J. Chem. Phys.* **137**, 22A530 (2012).
- [37] For the Floquet picture to approximately apply, the pulse envelope must not change too drastically during one optical cycle of the laser. For the H_2^+ -like model, where the one-photon resonance is reached very quickly, the approximate validity of the Floquet picture is questionable. To counter this, we use the Na_2^+ -like model with a larger nuclear mass in this scenario. The slower nuclear dynamics allows us to stretch the pulse envelope, fitting much more optical cycles into it.
- [38] W. B. Case, *Am. J. Phys.* **76**, 937 (2008).